

OPEN ACCESS

## Effect of Lithiation upon the Shear Strength of NMC811 Single Crystals

To cite this article: Joe C. Stallard *et al* 2022 *J. Electrochem. Soc.* **169** 040511

View the [article online](#) for updates and enhancements.

### You may also like

- [Impact of Graphite Materials on the Lifetime of NMC811/Graphite Pouch Cells: Part II. Long-Term Cycling, Stack Pressure Growth, Isothermal Microcalorimetry, and Lifetime Projection](#)  
A. Eldesoky, E. R. Logan, A. J. Louli et al.
- [Reducing Intrinsic Drawbacks of Ni-rich Layered Oxide Cathode Materials with a Dry Coating Concept of Quasi-solid Nanomaterials towards High-performance Cylindrical Li-ion Batteries](#)  
Poramane Chiochan, Chonticha Jangsan, Nichakarn Anansuksawat et al.
- [Lithium Difluoro\(dioxalato\) Phosphate as an Electrolyte Additive for NMC811/Graphite Li-ion Pouch Cells](#)  
Wentao Song, Roby Gauthier, Tina Taskovic et al.



### Your Lab in a Box!

The PAT-Tester-i-16: All you need for Battery Material Testing.

- ✓ All-in-One Solution with integrated Temperature Chamber!
- ✓ Cableless Connection for Battery Test Cells!
- ✓ Fully featured Multichannel Potentiostat / Galvanostat / EIS!

[www.el-cell.com](http://www.el-cell.com) +49 40 79012-734 [sales@el-cell.com](mailto:sales@el-cell.com)

**EL-CELL**<sup>®</sup>  
electrochemical test equipment





# Effect of Lithiation upon the Shear Strength of NMC811 Single Crystals

Joe C. Stallard,<sup>1,2</sup> Sundeep Vema,<sup>1,2,3,\*</sup> David S. Hall,<sup>2,3,\*</sup> Anthony R. Dennis,<sup>1</sup> Megan E. Penrod,<sup>2,3</sup> Clare P. Grey,<sup>2,3,\*\*</sup> Vikram S. Deshpande,<sup>1,2</sup> and Norman A. Fleck<sup>1,2,z</sup>

<sup>1</sup>Department of Engineering, University of Cambridge, CB2 1PZ, United Kingdom

<sup>2</sup>The Faraday Institution, Quad One, Harwell Campus, Didcot, OX11 0RA, United Kingdom

<sup>3</sup>Department of Chemistry, University of Cambridge, Cambridge, CB2 1EW, United Kingdom

An experimental protocol is developed to measure the shear strength of NMC811 single crystals within the cathode of a lithium-ion cell. The cathode is placed upon a set of thick metallic substrates that possess a wide range of indentation hardness. For each choice of substrate, the top surface of the cathode is indented by a Vickers indenter to a sufficient depth that the cathode layer is subjected to an approximately spatially uniform compressive normal traction equal to the hardness of the substrate. The sensitivity of plastic flow and fracture of the single crystals to substrate hardness is determined by observation of the particles in the indented top surface of the cathode using a scanning electron microscope. It is found that the shear strength of fully lithiated NMC811 single crystals along their basal plane is  $86 \pm 12$  MPa, and decreases to  $39 \pm 5$  MPa upon cell charging (delithiation of the cathode). This implies that particle slip and fracture will occur under mild mechanical loading, for example by calendaring during manufacture and by electrical cycling of the compacted cathode. The indentation protocol developed here has application to a wide range of single crystal cathode materials.

© 2022 The Author(s). Published on behalf of The Electrochemical Society by IOP Publishing Limited. This is an open access article distributed under the terms of the Creative Commons Attribution 4.0 License (CC BY, <http://creativecommons.org/licenses/by/4.0/>), which permits unrestricted reuse of the work in any medium, provided the original work is properly cited. [DOI: 10.1149/1945-7111/ac6244]



Manuscript submitted January 6, 2022; revised manuscript received February 23, 2022. Published April 6, 2022.

Supplementary material for this article is available [online](#)

Layered oxides of composition  $\text{Li}_y\text{Ni}_x\text{Mn}_z\text{Co}_{(1-x-z)}\text{O}_2$  (NMC), in which the lithium content  $y$  varies in the range  $0 < y < 1$ , are widely used as the active storage material in lithium ion battery (LIB) cathodes.<sup>1,2</sup> Typically, NMC cathodes are manufactured by the tape-casting of a solvent-based slurry of NMC particles, polymeric matrix and carbon powder onto an aluminium film, which serves as a current collector.<sup>3</sup> Evaporation of the solvent leaves a porous cathode microstructure, with typical volume fraction of active storage material (in the pre-compacted state) between 0.40 and 0.60, and carbon-infiltrated polymer of volume fraction less than 0.1. The remaining 30%–50% of the cathode volume is porosity.<sup>3,4</sup>

A calendaring operation is often used to increase the particle packing density (and reduce the porosity) of the cathode. This reduces both cell volume and cell mass (by reducing the amount of encapsulation), and thereby increases the storage energy and the power capacity of the cell, per unit volume and per unit cell mass. Computed tomography (CT) studies of cathodes that comprise polycrystalline NMC particles have reported that the calendaring operation can lead to significant particle fracture and pulverisation.<sup>5,6</sup> For typical NMC cathodes, the increase in achievable charging rate after calendaring is ascribed to an enhanced effective electrical conductivity of the cathode composite.<sup>3,7–9</sup> Calendaring helps to reduce interfacial resistance between active material and current collector and hold the whole structure together during extended cycling.

The need to extend cycle life of NMC cathodes has led to the recent development of so-called single crystal cathodes, whereby NMC particles comprise single domain, micron-sized particles (and bi-crystals).<sup>10,11</sup> Previously, NMC cathode material existed in the form of *primary* particles of diameter between 0.1  $\mu\text{m}$  and 1  $\mu\text{m}$ , agglomerated into polycrystalline *secondary* particles of diameter<sup>12–15</sup> between 3  $\mu\text{m}$  and 20  $\mu\text{m}$ . These secondary particles suffer from the drawback that lithiation and delithiation induce intergranular fracture between the primary grains. Intercalation of Li ions induces anisotropic swelling within each primary grain, and the

elastic constraint imposed by neighbouring primary grains leads to stressing of the grains and of the grain boundaries. These self-equilibrating stresses may be of sufficient magnitude to induce fracture of the grain boundaries between primary grains over a charge cycle.<sup>16</sup> In contrast, much lower stresses are generated in single crystal cathodes due to the reduced elastic constraint between neighbouring single crystals. This might be the reason that single crystal cathodes have exceptional resistance to degradation,<sup>17</sup> retaining over 90% of their initial capacity over 4,000 full cycles.

A typical single crystal of NMC811 is sketched in Fig. 1a. It has the  $R\bar{3}m$  space group, and exists as a single phase.<sup>18</sup> The prismatic direction is denoted by the unit vector  $c$ . The mutually orthogonal  $a$  and  $b$  lattice directions of the basal plane sit in the prismatic plane of the particle. Thus, the orthonormal vectors ( $a$ ,  $b$ ,  $c$ ) are aligned with the principal directions of the lattice. It is generally recognised that the unit cell dimensions of NMC811 are sensitive to the state of charge. The lattice parameters  $a$  and  $c$  are plotted against lithium occupancy<sup>18</sup>  $y$  in Fig. 1b; both  $a$  and  $c$  are normalised by their values in a fully lithiated state, as denoted by  $a_0$  and  $c_0$ . There is no need to consider the third lattice constant  $b$  as  $b/b_0 = a/a_0$  in the basal plane of the unit cell. During delithiation (decreasing  $y$ ),  $c/c_0$  initially rises, and then subsequently falls for  $y < 0.3$ , whereas  $a/a_0$  decreases with decreasing  $y$ .

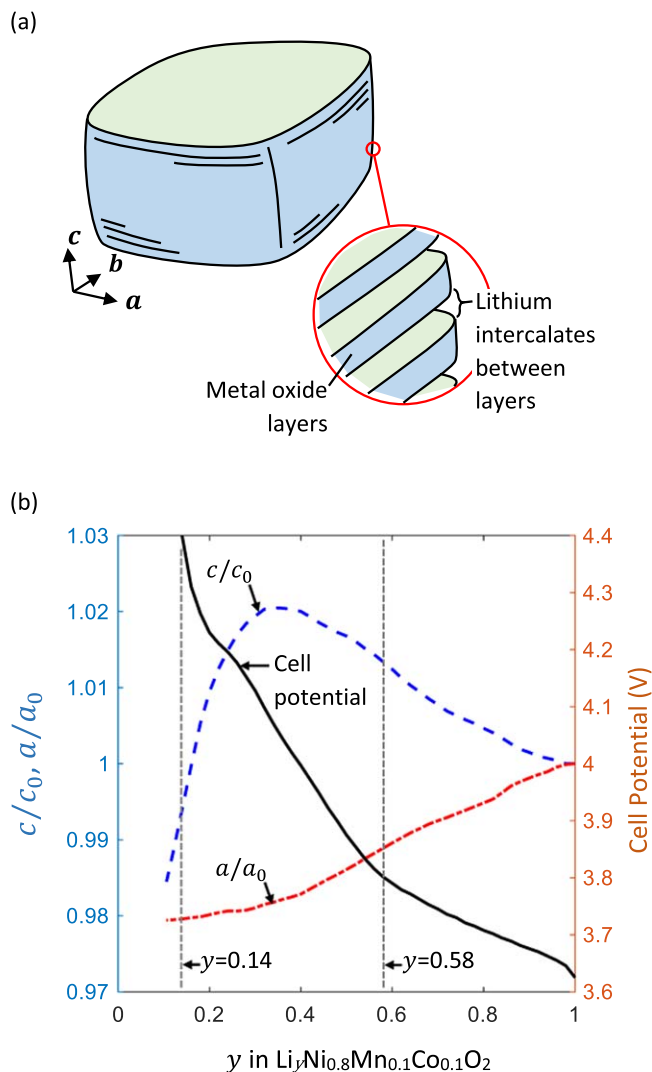
The mechanical properties of NMC single crystals have not been reported in the open literature to the best of the authors' knowledge. Single pillar compression experiments have been performed on other layered oxides such as  $\text{Li}_y\text{CoO}_2$  (LCO). For example, Feng et al.<sup>19</sup> have found that the uniaxial compressive strength of an isolated LCO crystal is on the order of 2–4 GPa in the initial, uncycled state. They observed two deformation modes of the pristine LCO: (i) a shear mode on an inclined plane at an axial stress of 2 GPa, see their Fig. 4b; and (ii) uniform plastic straining by dislocation-mediated plasticity, at an axial stress of 4 GPa, see their Fig. 4a. A possible interpretation for these modes is that plastic deformation may occur via two mechanisms, as follows:

**Mechanism (i).** Single slip occurs on the prismatic plane of the layered oxide when the critically-resolved shear stress on a slip plane, inclined to the loading axis in a single pillar test, attains a value on the order of 100 MPa, corresponding to an axial stress of 2 GPa. This inclined plane is referred to as a “cleavage plane” rather

\*Electrochemical Society Member.

\*\*Electrochemical Society Fellow.

<sup>z</sup>E-mail: [naf1@eng.cam.ac.uk](mailto:naf1@eng.cam.ac.uk)



**Figure 1.** (a) Sketch of an NMC811 single crystal, illustrating the prismatic direction  $c$  and the layered atomic structure. (b) Sensitivity of the normalised unit cell dimensions<sup>18</sup>  $a/a_0$  and  $c/c_0$  and cell potential to lithium content  $y$  for single crystal NMC811 cathodes during the first charge at  $10 \text{ mAh g}^{-1}$ .

than a slip plane.<sup>19</sup> This motivates the present study: does single slip occur in layered oxides at values of shear stress on the order of tens or hundreds of MPa rather than several GPa? Such slip at low resolved shear stress is consistent with recent observations and calculations for NMC811 single-crystal cathodes under cyclic electrical loading:<sup>20</sup> slip bands were observed in NMC811 single crystals under electrochemical cycling, and the predicted shear stresses within the crystals due to charge and discharge did not exceed a few hundred MPa.

**Mechanism (ii).** Additional, secondary slip systems can be envisaged, but these slip systems will be much stronger than the primary slip system on the basal plane; activation of several of these additional slip systems gives rise to uniform plastic straining by dislocation-mediated plasticity. Measurements<sup>19</sup> suggest that this occurs at an axial stress of 4 GPa.

The measured indentation hardness<sup>15,21</sup> of polycrystalline NMC secondary particles is in the range 5–8 GPa, but it is a challenge to relate this macroscopic quantity to the shear strength of the primary grains. The usual interpretation that the macroscopic hardness of a polycrystal equals three times its uniaxial strength is only valid for a crystal that possesses at least 5 slip systems.<sup>22</sup> Layered polycrystalline ceramics have a much-reduced availability of slip systems, and

consequently their macroscopic hardness may be dictated by the activation of secondary slip systems of slip strength much above that of the basal plane, or by the granular flow of the polycrystalline ceramic after it has suffered extensive fragmentation along its grain boundaries.

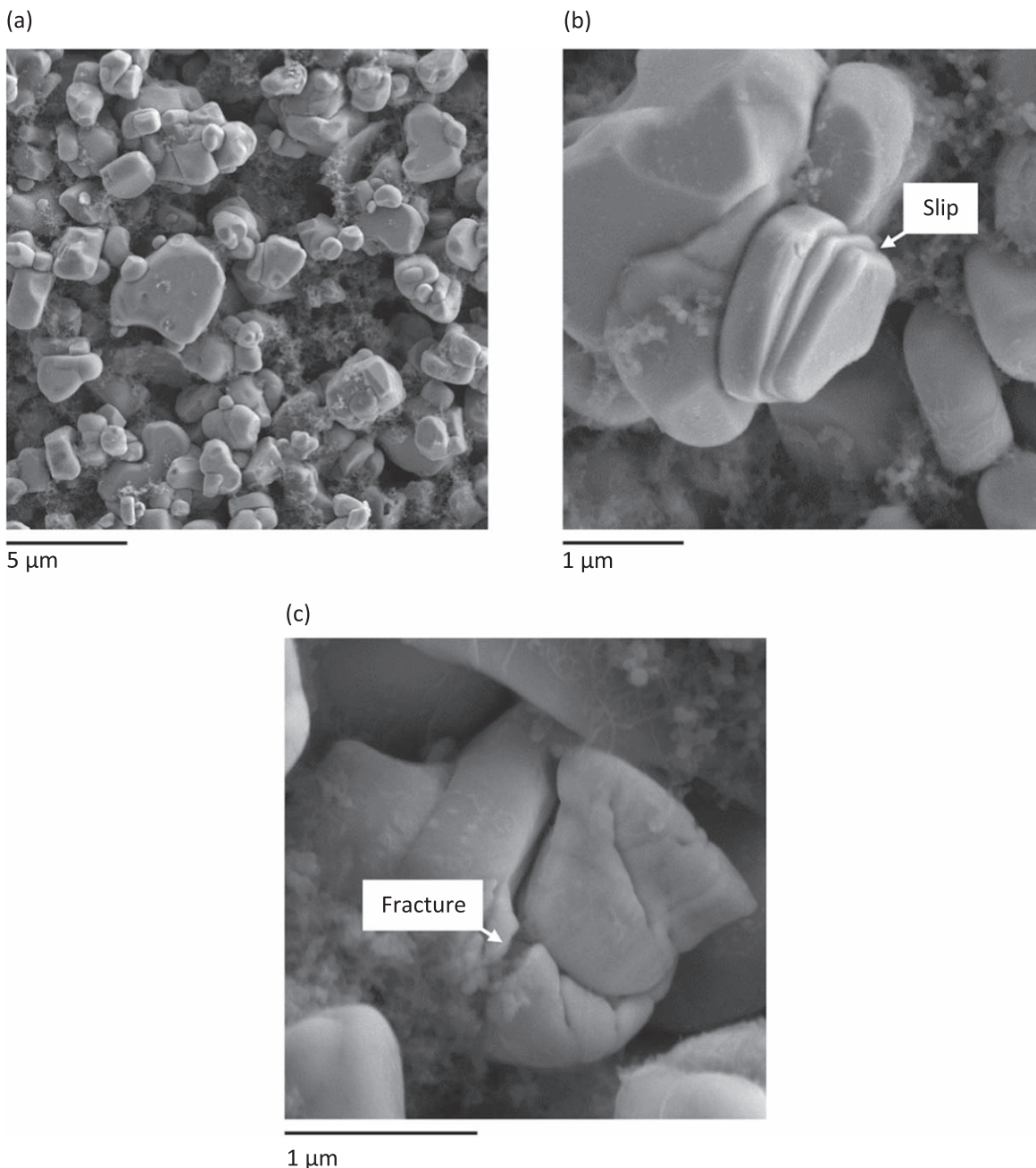
**Scope of study.**—In the present study, an indentation-based test protocol is developed to measure the basal shear strength of a large number of fully lithiated ( $y = 1$ ) NMC811 single crystals in situ within a cathode layer. The imposed compressive stress on the NMC single crystals is set by the indentation hardness of the underlying metallic substrate, and the number fraction of single crystals that have undergone plastic slip and fracture is observed post-indentation. The test procedure is then used to determine the sensitivity of the NMC811 single crystal strength to lithium occupancy  $y$ , by repeating the experiments on cathodes that have been extracted from Li ion cells in various states of charge.

### Test Protocol: Indentation of an NMC811 Cathode upon a Substrate of Defined Hardness

**Test material.**—NMC811 cathodes (obtained from Li-Fun Technology Corporation Ltd., Hunan Province, P.R. China) comprise a porous microstructure in the tape cast but uncalendered state. The cathode active material is cast upon the current collector at an areal density of  $0.167 \text{ kg m}^{-2}$ . The as-received, fully lithiated ( $y = 1$ ) cathode and aluminium backing are of thickness  $65 \mu\text{m}$  and  $15 \mu\text{m}$  respectively, as measured by CT scanning (Xradia 520 Versa, Zeiss Ltd., Cambridgeshire, UK). Upon taking the density<sup>23,24</sup> of  $\text{LiNi}_{0.8}\text{Mn}_{0.1}\text{Co}_{0.1}\text{O}_2$  as  $4780 \text{ kg m}^{-3}$  it follows that the NMC cathode particles comprise 54% of the cathode volume; the remainder is 7% graphite-infiltrated polymer binder, and 39% porosity, which allows for infiltration by a liquid electrolyte. A plan view of the cathode microstructure is shown in Fig. 2a, as observed in a scanning electron microscope (SEM) (MIRA3 FEG-SEM, TESCAN-UK Ltd., Cambridgeshire, UK). Many of the particles are prismatic in shape and it is assumed that the  $c$ -axis of the layered crystals is aligned with the prismatic direction.

The SEM images of the fully lithiated ( $y = 1$ ) cathode microstructure reveal that most of the single crystal particles have a diameter in the range  $1 \mu\text{m}$  to  $3 \mu\text{m}$ . A small proportion of them contain slip bands or multiple fractures in the pristine state, examples of which are shown in Figs. 2b and 2c, respectively. The proportion of cathode particles with slip bands and fractures was measured by obtaining ten SEM images of the cathode microstructure at a fixed magnification of  $\times 10^4$ : each image contained about 100 particles. From these images, an average number fraction of 0.88 of the particles contain neither slip bands nor cracks. The number fraction with slip bands, but no indication of fracture, was 0.11, and the remaining number fraction of particles ( $<0.01$ ) had either single or multiple fractures, or a combination of fractures and slip bands.

The lithium content  $y$  of the NMC was varied by assembling Li-ion cells, using the as-received cathode, a graphite anode, and a liquid electrolyte; full details are reported in a previous study.<sup>18</sup> In brief, additional values of  $y = 0.58$  and  $y = 0.14$  were achieved as follows. A charging current of  $1/20$  of the full cell charge capacity per hour ( $C/20$ ) was used until cell voltages of 3.8 V and 4.4 V were obtained, which correspond to  $y = 0.58$  and  $y = 0.14$ , respectively.<sup>18</sup> These two values of voltage were held fixed for 20 h, after which the cells were disconnected and disassembled, all within a sealed glovebox under an argon atmosphere. The electrolyte was removed by rinsing the cathodes with dimethyl carbonate, followed by drying under vacuum. We shall subsequently show that this procedure, involving a low charging current to delithiate the cathode, does not change the number fraction of slipped and fractured grains prior to the indentation tests.



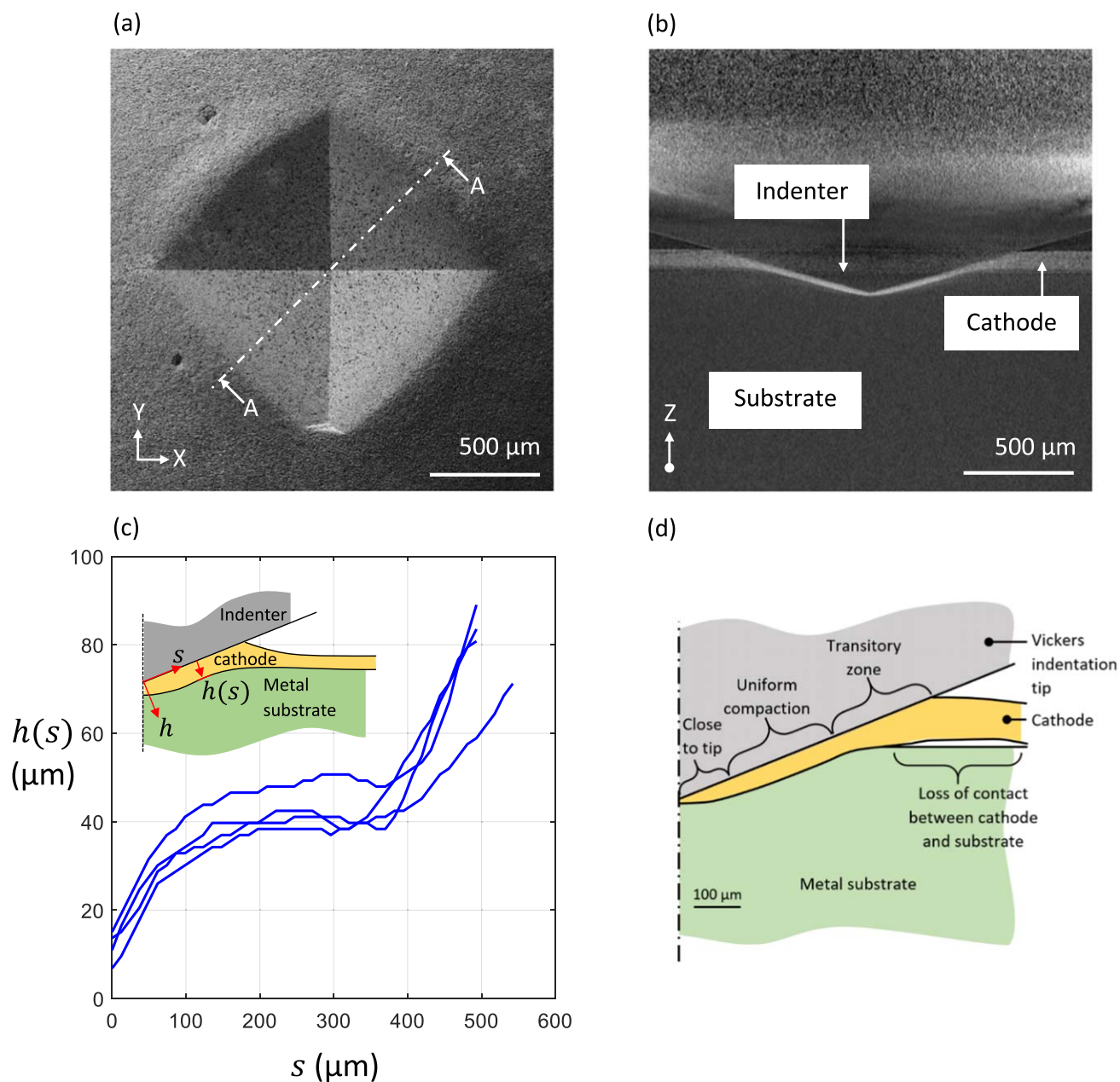
**Figure 2.** Images of individual single crystal cathodes particles obtained with a scanning electron microscope: (a) the microstructure of a fully lithiated ( $y = 1$ ) single-crystal NMC811 cathode in plan view. Single crystal cathode particles with evidence of (b) slip planes and (c) fracture.

**Indentation tests.**—The indentation method used in this study to measure the yield and fracture response of single crystal NMC811 particles is now discussed. Particles within the cathode were subjected to a macroscopic uniform compressive stress, as dictated by the indentation hardness of the chosen substrates. The hardness was varied by a factor of almost 20 by suitable choice of substrate, from annealed lead to work-hardened copper. It is assumed that slip or fracture of any particle occurs when the resolved shear stress on the basal slip plane of that particle attains a critical value. A mechanics analysis is used to determine the value of this critically resolved shear stress, and to estimate the distribution function of particle orientation. The details are given below.

The stress field created by indentation of an elastic, ideally plastic solid by a Vickers indenter, with a surface layer absent, has already been detailed by finite element simulations.<sup>25,26</sup> It is found that the compressive traction along the flanks of the indenter is almost

uniform in space, and of magnitude about three times the uniaxial yield strength of the substrate. A small elevation in traction occurs at the tip of the indenter<sup>27</sup> and along the sharp edges between the facets<sup>28</sup> but their effects upon the indenter load is negligible.<sup>25–28</sup> If a thin film exists between the substrate and the indentation tip, and the indentation depth is much greater than the film thickness, then the indentation pressure is hardly perturbed by the presence of the thin film.<sup>29,30</sup>

Conical indentation has the advantage that the indenter has no intrinsic length scale, only a characteristic angle of indenter.<sup>31</sup> The representative strain beneath the indenter is constant: the strain state of a semi-infinite solid indented by a conical indenter immediately achieves a steady state that depends only upon the position of a material point normalised by the current contact radius  $a$ . The strain field has a singularity at the tip of the cone. In contrast, a flat bottomed indenter (such as a frictionless circular punch) has a



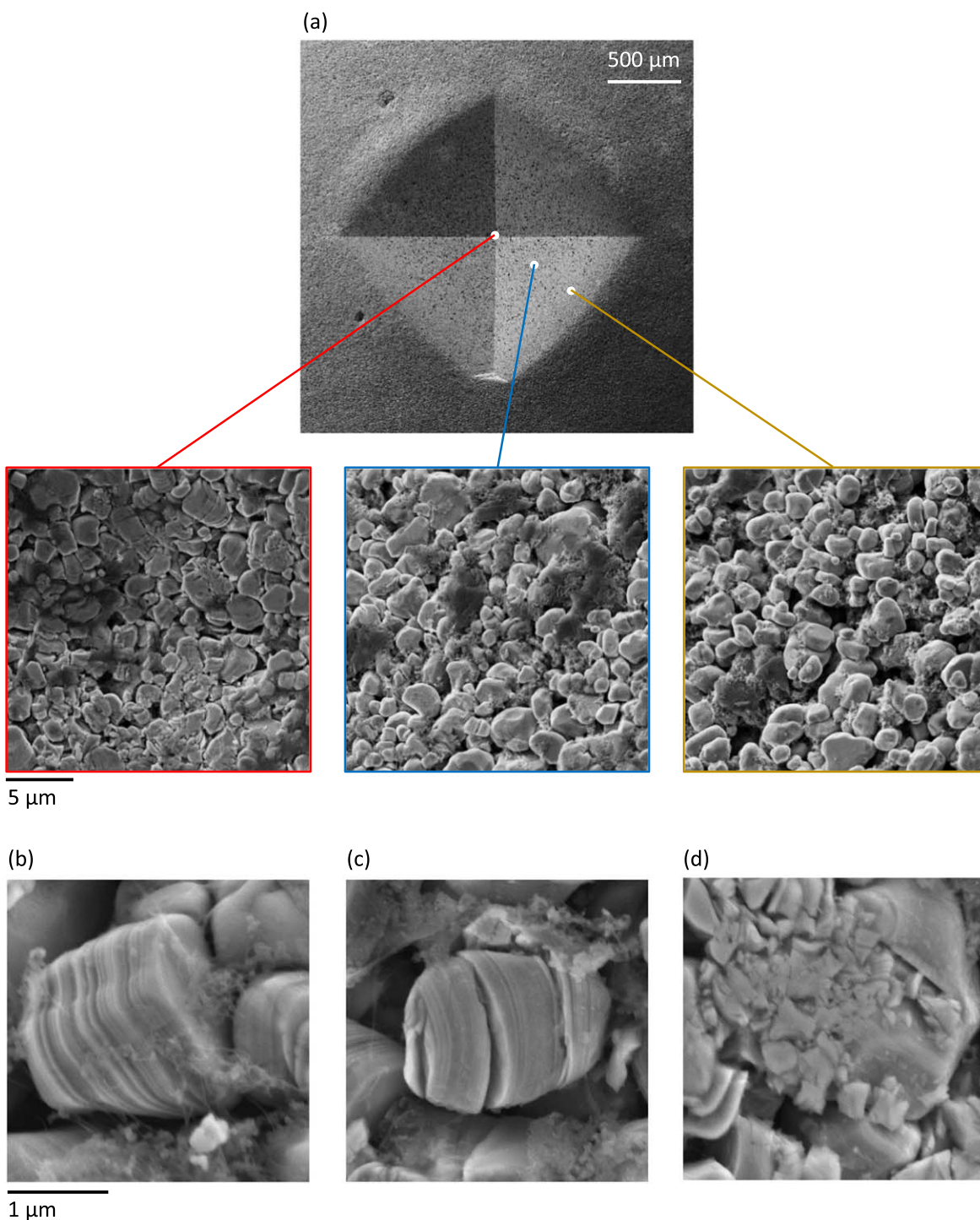
**Figure 3.** (a) Image of a fully lithiated ( $y = 1$ ) cathode after indentation by a load of 120 N upon an annealed aluminium substrate. (b) Image of the cathode during indentation, along the cross section A–A, as identified in (a). (c) Plot of cathode thickness measured perpendicular to the indenter flank as a function of distances from the tip, and (d) zones of deformation of the cathode. Image (a) is obtained from SEM, image (b) and the plots (c) and (d) are obtained from in situ X-ray computed tomography at a fixed load of 120 N.

characteristic length scale defined by the punch radius. Further, a singular strain state exists at the edge of contact which is identical to that of a crack singularity. The magnitude of this strain singularity increases with indentation depth. Likewise, the strain at any point beneath the punch will increase with increasing indentation depth, and so a steady state is not attained.

A series of indentation tests were performed with the cathode supported by flat, polished metal substrates of thickness 6 mm or greater. The tests were performed using a Vickers diamond indentation tip (UK Calibrations Ltd., Herefordshire, UK) affixed to the crosshead of a screw-drive mechanical test machine (5944 test machine with 2 kN load cell, Instron Ltd., Buckinghamshire, UK). The test machine and indentation experiments were performed in an

inert argon gas atmosphere within a glovebox (M.Braun Inertgas-systeme GMBH, Garching, Germany), in which the concentrations of oxygen and water were both maintained at less than 0.1 ppm. The diamond Vickers tip has the shape of a square pyramid, in which the four triangular facets are inclined at an angle of  $22^\circ$  from the base, and the tip radius equals  $2\text{ }\mu\text{m}$ . The indentation tests were performed at a velocity of  $2\text{ }\mu\text{m s}^{-1}$  until a specified indentation load  $P_I$  was obtained; the tip was then withdrawn from the sample.

The hardness of the metallic substrates was varied from 50 MPa to 946 MPa by a suitable selection of metals and alloys including lead, tin solder, aluminium and copper, and subjecting them to various heat treatments and work hardening treatments. Details of the alloys, their composition, heat treatment, and work hardening

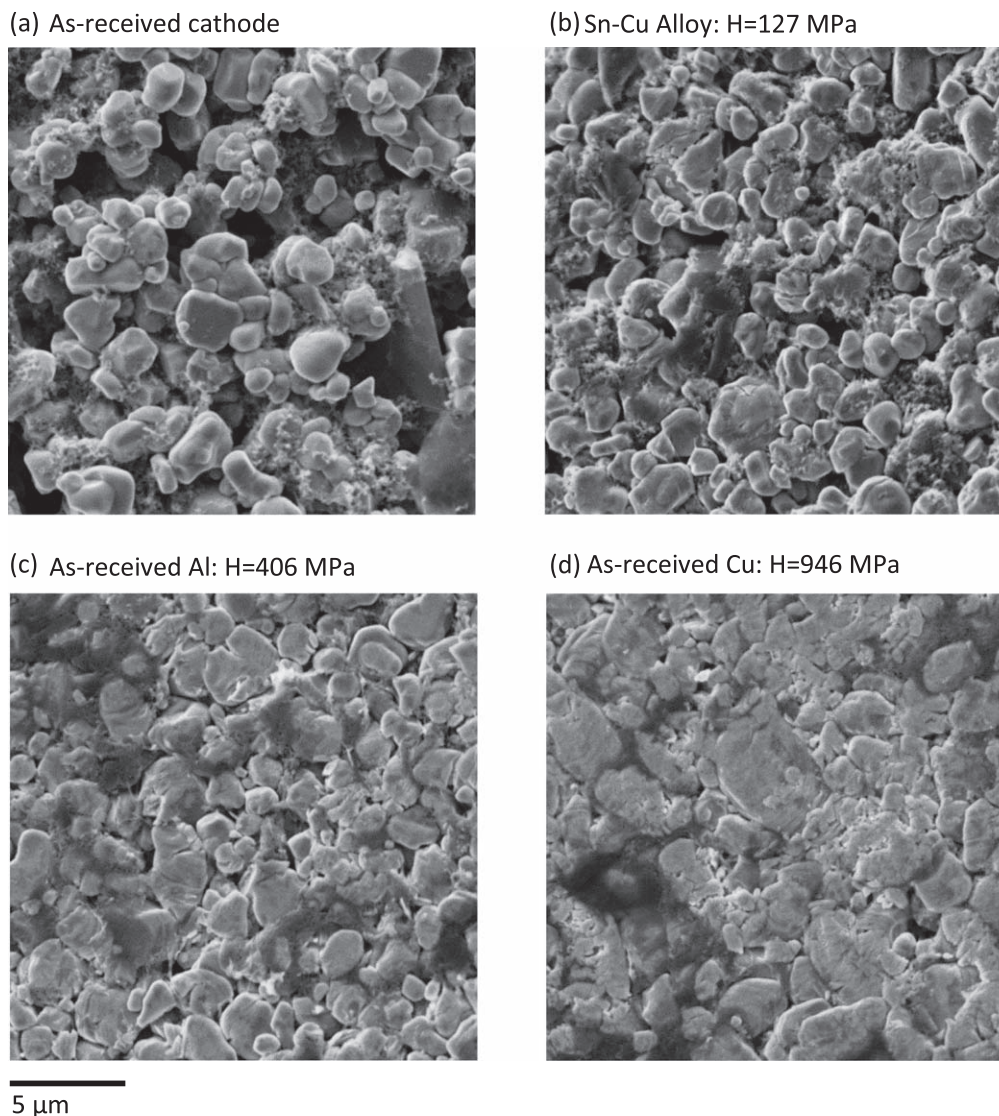


**Figure 4.** (a) Variation in the degree of compaction within an indent of a fully lithiated ( $y = 1$ ) cathode. Images of (b) particles with slip bands, and (c)–(d) of particles with various combinations of slip bands and fracture.

treatment are listed in Table SI of the supplementary information (available online at [stacks.iop.org/JES/169/040511/mmedia](https://stacks.iop.org/JES/169/040511/mmedia)), along with their measured hardness  $H$  absent a cathode layer:  $H$  equals the indentation pressure on the as-measured projected area of indent  $A_P$ , and is related to the indentation load  $P_I$  by  $H = P_I/A_P$ .

In a preliminary set of tests with an aluminium substrate of hardness  $H = 283$  MPa, a set of 10 indents were made on a fully lithiated cathode with fixed indentation load,  $P_I = 155$  N. The mean projected area of the residual indents formed in the cathode was

$1.04 \text{ mm}^2$ ; variation was at most 6% of this mean value. This confirmed that the cathode material was uniform in properties. Further cathode indentation experiments using substrates of annealed copper ( $H = 436$  MPa) and tin-copper alloy ( $H = 127$  MPa) revealed that the observed hardness was independent of indentation depth provided the indentation depth was greater than 2.5 times the coating thickness. The significance of pile-up vs sink-in is accounted for by making visual observation of the projected area of the indent. In all subsequent experiments, cathodes were indented with loads  $P_I$



**Figure 5.** Microstructure of the as-received, fully lithiated ( $y = 1$ ) cathode (a) and indented cathodes (b)–(d) imaged after indentation upon substrates of increasing hardness. Images of the indented cathode are obtained at a distance of  $\sqrt{A_P}/4$  from the apex of each indent and equidistant between two edges. All images are obtained by SEM.

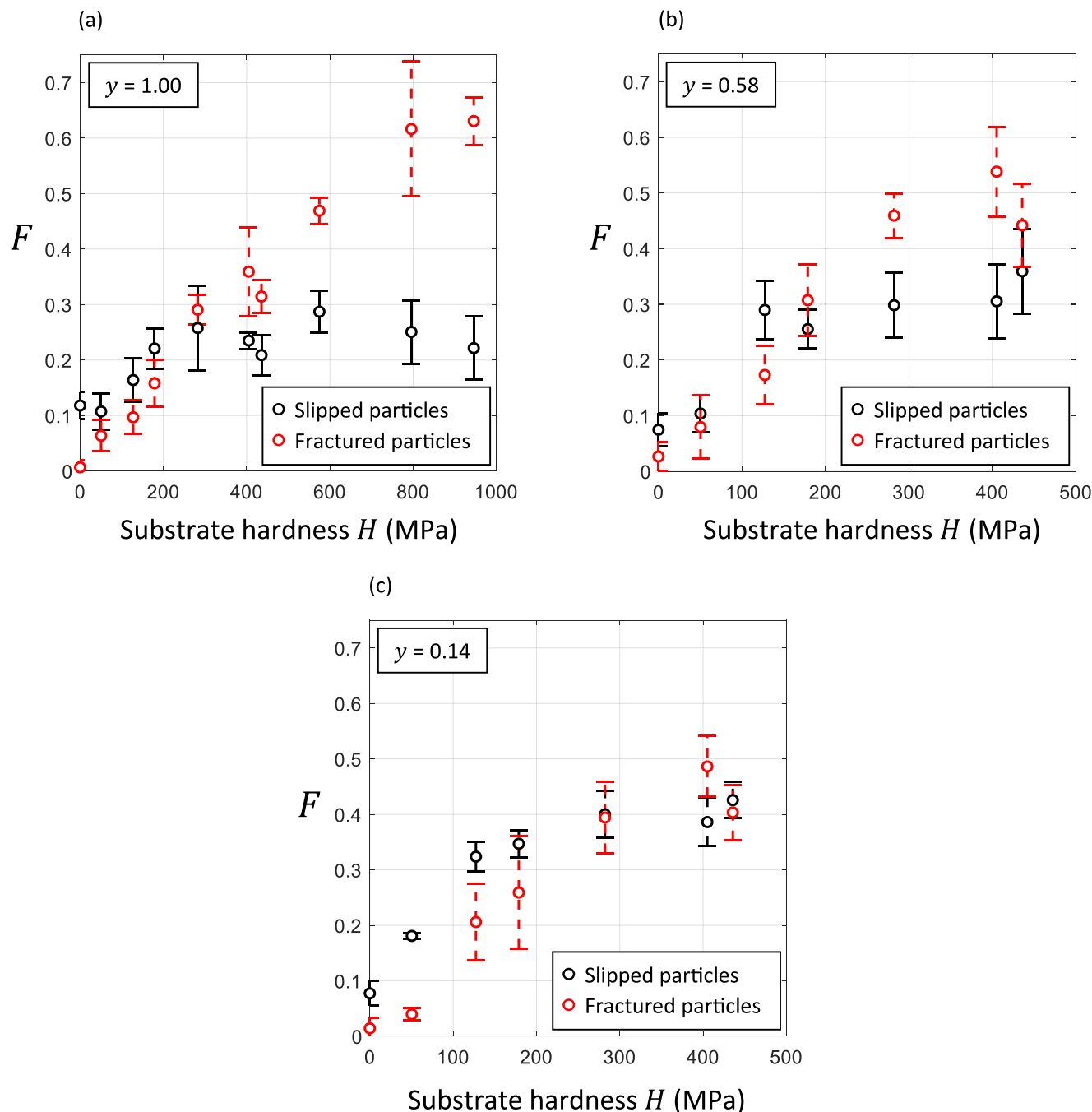
in the range  $25 \text{ N} \leq P_f \leq 520 \text{ N}$ , depending upon the hardness of the substrate: higher indentation loads were imposed on cathodes that rested on harder substrates to ensure that the indent displacement was always between 3.0 and 3.5 times the thickness of the cathode, and that all indents were of approximately equal area.

**Deformation of cathode due to indentation.**—An image of a representative indent in a fully lithiated ( $y = 1$ ) cathode is shown in Fig. 3a, for an annealed aluminium substrate of hardness  $H = 179 \text{ MPa}$  and an indentation load  $P_f = 12 \text{ N}$ . The thickness profile of the cathode during indentation was obtained by making use of a custom-built, in situ indentation rig inside a CT scanner. Sufficient X-ray penetration for practical imaging was achieved at an acceleration voltage of 80 kV by employing a polished annealed aluminium cylinder of diameter 10 mm as the substrate. A computed tomography scan of the cross-section of the cathode during indentation is shown in Fig. 3b at an indent load of 120 N. The section is made on plane A–A, as defined in the SEM top view of the indented cathode surface in Fig. 3a. The thickness  $h$  is plotted against distance  $s$  from the indenter apex in Fig. 3c, and the interpretation of the deformation state of the cathode layer, sandwiched between the indenter and the substrate, is given in Fig. 3d. When the indentation

depth of the Vickers indenter exceeds twice the cathode thickness, the average normal compressive traction<sup>29</sup> on the layer in contact with the indenter is close to that of the substrate hardness  $H$ . This is confirmed by the accompanying observation that the indent size of the substrate beneath the cathode layer is close to the indent size for indentation of the substrate alone at an identical load. Also, no delamination of the coating from the current collector was observed beneath the indenter.

Post-indentation SEM imaging of the compressed microstructure of the fully lithiated cathode is shown in Fig. 4a due to the indentation performed as reported in Fig. 3. The degree of compaction of the cathode layer varies from high compaction at the apex, to a uniform state of moderate compaction along the flanks, to a low degree of compaction at the periphery of the indent. No compaction was evident in the pristine cathode material external to the indent. Examples of individual particles with signs of plastic deformation are shown in Figs. 4b–4d. The particles may display slip bands alone (Fig. 4b), or may display a combination of slip bands and cracks (Figs. 4c and 4d).

Confirmation that the substrate hardness dictates the compressive stress to which a cathode is subjected in indentation testing is illustrated by images of indented, fully lithiated cathode



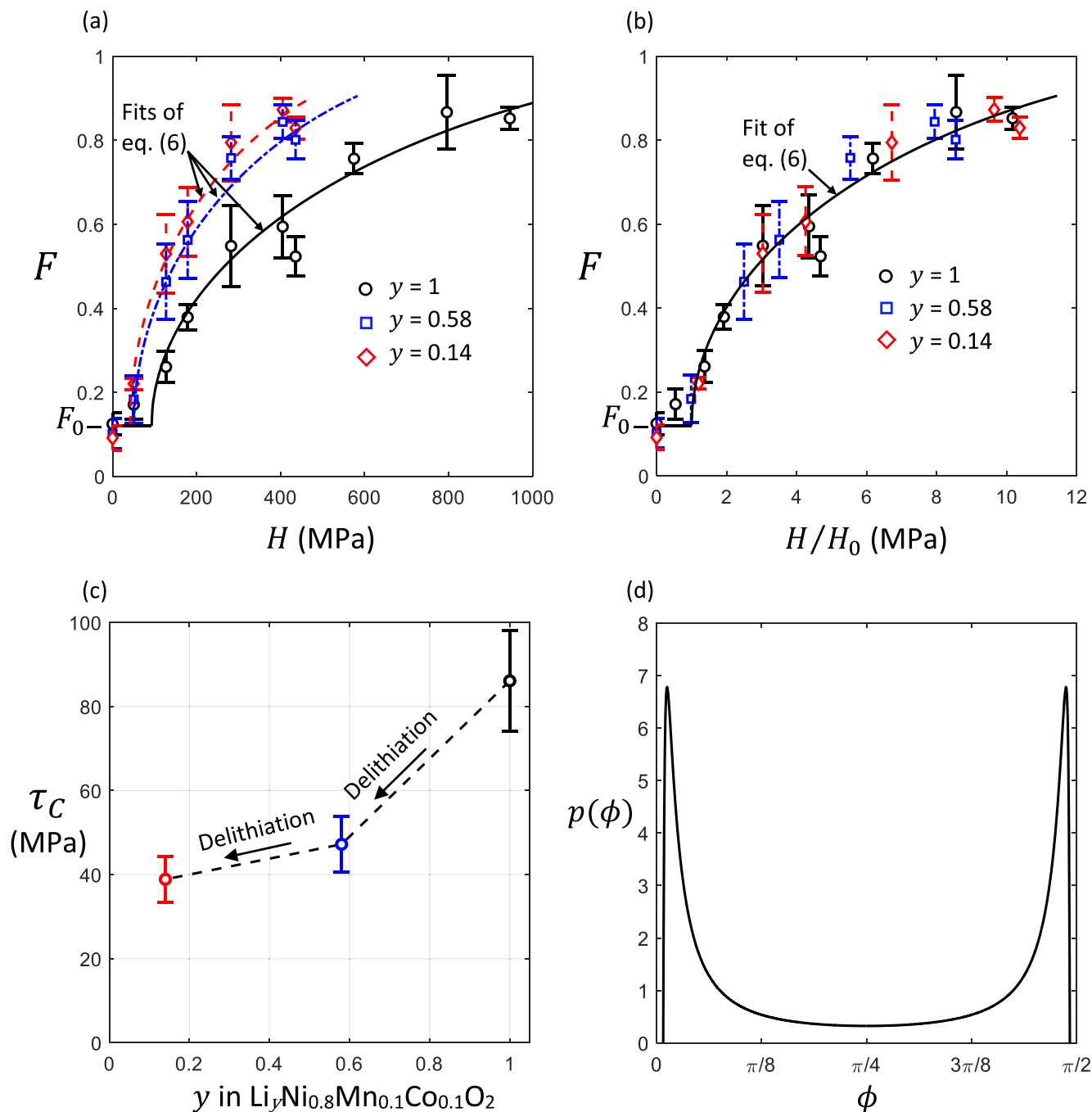
**Figure 6.** The measured number fraction  $F$  of particles that have slipped and/or fractured counted from images of the indented cathode microstructure are plotted against the substrate hardness  $H$  for a lithium occupancy of (a)  $y = 1.00$ ; (b) 0.58 and (c) 0.14. Bars included in the plotted data represent one standard deviation from the mean number fractions.

microstructure, as shown in Fig. 5. All images were obtained at a radial distance  $\sqrt{A_P}/4$  from the apex of each indent, which is approximately mid-way along the tip flanks of uniform compaction pressure zone as identified in Fig. 3d. The degree of compaction in the cathode microstructure at this location increases with increasing substrate hardness  $H$ .

**The number fraction of single crystals that yield and/or fracture as a function of indentation pressure.**—The effect of the level of pressure on the active material particles was assessed by imaging the microstructure of the indented cathodes at a radial distance  $\sqrt{A_P}/4$

from the apex of each indent. From these images, the number fraction of particles that possess slip bands, or various combinations of fractures and/or slip bands, was measured by particle counting. All images were obtained using the same magnification of  $\times 10^4$  as employed for assessing the fraction of particles with slip bands or fractures in the pristine cathode. The number of particles counted in each image was on the order of 100.

To assess the degree of repeatability in these experiments, one image was obtained of each of the ten indentations made in preliminary experimentation with load  $P_I = 155$  N on an aluminium substrate of hardness  $H = 283$  MPa. From these images, the mean fraction of particles that were cracked or slipped was 0.49, and the



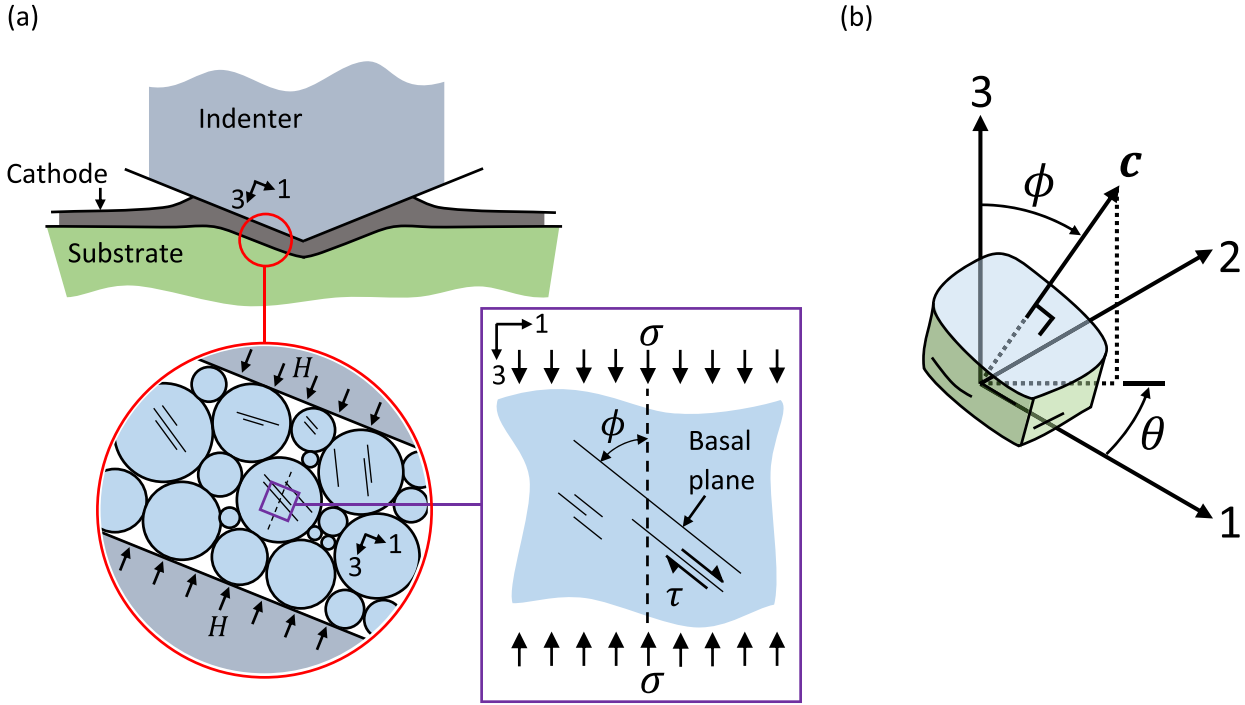
**Figure 7.** The measured number fraction  $F$  of particles that have slipped and/or fractured vs (a) substrate hardness  $H$ , and (b) vs normalised substrate hardness  $H/H_0$ . (c) Average basal shear strength vs degree of lithiation as deduced from the slip model. (d) The orientation function of particles within the cathode  $p(\phi)$  as deduced from the fit for  $F(H/H_0)$ .

standard deviation of this fraction was 0.04. For the experiments detailed below, a single indent was performed for any given choice of substrate and any given state of charge of cathode. Four images were obtained from each of these indents for particle counting, one at the centre of each of the indentation faces.

The fraction of slipped and fractured particles counted from indented cathodes are plotted in Figs. 6a–6c, against the hardness of the metal substrate, for cathodes in a fully lithiated state (for which  $y = 1$ ), and two other states of charge,  $y = 0.58$  and  $y = 0.14$ . The value  $y = 0.58$  is not at the peak value of  $c/c_0$  but does give rise to a noticeably expanded  $c$  lattice parameter whereas the value  $y = 0.14$  is close to the fully

delithiated state. The cell potential, along with the states of  $y = 1$ , 0.58 and 0.14, are included in Fig. 1b; the cell potential rises as the lithium occupancy  $y$  decreases during cell charge.

For all cathodes ( $y = 0.14$ , 0.58 and 1), the number fraction of particles that display both slip and fracture increase with increasing pressure (as defined by the hardness of the substrate). In the case of the fully lithiated ( $y = 1$ ) particles (Fig. 6a), the fraction of particles that possess slip bands alone initially rises with indentation pressure, up to a pressure of approximately 400 MPa. This number fraction then decreases under increased indentation pressure, as many of the slipped particles proceed to fracture. A negligible proportion of



**Figure 8.** (a) Sketch of the cathode during indentation, with stresses at the cathode and particle level annotated. (b) The unit normal to the basal plane  $\mathbf{c}$ , and the angle of basal plane inclination  $\phi$  are relative to the 3-direction along which compressive tractions are applied in the indentation tests.

particles crack without slip. The slip plane is always parallel to the prismatic direction—that is parallel to the basal plane of the layered lattice.

A close connection between yield and fracture of the particles is evident, and consequently we introduce the number fraction  $F$  of particles that have slipped and/or fractured and write  $F$  as a function of hardness  $H$ . The observed response  $F(H)$  is plotted in Fig. 7 for  $y = 0.14, 0.58$  and  $1$ . For all three states of lithiation  $y$ ,  $F$  equals an initial value  $F_0 = 0.12$  in the pristine state to within experimental scatter, confirming that charging the cell at C/20 does not induce fracture/slip in the NMC crystals. The number fraction  $F$  is maintained at  $F = F_0$  as  $H$  is increased up to a threshold value  $H_0$ , and then  $F$  increases sharply for  $H > H_0$ . Note from Fig. 7 that the value of  $H_0$  is sensitive to the value of  $y$ , such that  $H_0 = 93$  MPa, 51 MPa and 42 MPa for  $y = 1, 0.58$  and  $0.14$  respectively. It is also noted that the dependence of  $F$  upon  $H/H_0$  is independent of the lithiation state  $y$ ; see Fig. 7b. This observation helps motivate a mechanics model to explain the micromechanical origins of  $F(H/H_0)$  as detailed in the following section.

### An Estimation of Basal Plane Shear Strength

It remains to relate the average compressive traction (which equals the substrate hardness  $H$ ) on the surface of the cathode layer to the shear stress on the crystallographic basal plane within the cathode particles. The cathode microstructure and stresses within it are sketched in Fig. 8a. The simplest approach is to employ the Reuss lower bound assumption such that the uniaxial stress  $\sigma$  within each crystal is related to the substrate hardness  $H$  and cathode porosity  $f$  according to

$$\sigma = H/(1 - f) \quad [1]$$

The porosity of the uncalendered material is  $f = 0.46$  upon treating both the 7% carbon-infiltrated polymer binder, and the 39% air as porosity. The resolved shear stress  $\tau$  on any basal plane, with unit normal  $\mathbf{c}$  inclined at an angle  $\phi$  to the loading direction (defined in Fig. 8b) is related to the hardness  $H$  via

$$\tau = \frac{H \sin 2\phi}{2(1 - f)} \quad [2]$$

Consequently, the resolved shear stress  $\tau$  vanishes for  $\phi = 0, \pi/2$  for any finite value of  $H$ . Between these limits,  $\tau$  rises towards a maximum value  $\tau^{\max}$  at a basal plane inclination of  $\phi = \pi/4$ .

The hardness  $H_0$  is defined as that which gives  $\tau^{\max} = \tau_C$ , where  $\tau_C$  is the shear strength of the basal plane. From (2) it follows that the value of hardness  $H_0 = 2(1 - f)\tau_C$  initiates yield of the most favourably oriented particles. It is further assumed that the degree of slip on the basal plane is limited by jamming of the slipped particle against its neighbours, so that, post-yield, the particle can bear a shear stress on the basal plane that exceeds  $\tau_C$ . Recall that we make no distinction between yield or fracture of a particle and simply refer to a particle as either “slipped” or “unslipped.”

Now consider the application of a pressure  $H > H_0$ . Then, all particles of orientation  $\phi$  in the range  $\phi_L < \phi < \phi_U$  will slip, where  $\phi_L < \pi/4 < \phi_U$ . The values of  $\phi_L$  and  $\phi_U$  are the two solutions for which  $\tau = \tau_C$ . The roots of (2) are symmetric about  $\phi = \pi/4$  such that  $\phi_L + \phi_U = \pi/2$ ; the larger root is denoted by  $\phi_U$  and satisfies

$$\sin 2\phi_U = \frac{2(1 - f)\tau_C}{H} = \frac{H_0}{H} \quad [3]$$

The lattice orientation of the basal plane of each particle, as defined by the unit normal  $\mathbf{c}$ , can be written in terms of the spherical co-ordinates  $(\phi, \theta)$ , as sketched in Fig. 8b. Consider the probability distribution function  $p(\mathbf{c})$  of the unit normal  $\mathbf{c}$  over a sphere of unit area  $S$ , (and of radius  $r = 1/(2\sqrt{\pi})$ ). For any suitably normalised probability density function  $p(\mathbf{c})$ , its integration over unit surface  $S$  equals unity,

$$\int_S p(\mathbf{c}) ds = 1. \quad [4]$$

Assume that the orientation of particles within the cathode is transversely isotropic within the plane of the cathode as a result of

the deposition process of the crystals during manufacture, such that  $p(c)$  is independent of  $\theta$  (Fig. 8b) and can thereby be written as  $p(\phi)$ . The cumulative number fraction  $F$  of slipped particles at any value of applied uniaxial stress  $\sigma$  is given by

$$F - F_0 = (1 - F_0) \int_{\frac{\pi}{2} - \phi_U}^{\phi_U} p(\phi) \sin \phi \, d\phi, \quad [5]$$

where  $F_0$  is the fraction of slipped particles in the initial pristine state. The indentation results of the present study can be used deliver the curve  $F(H)$ , upon noting that  $\sigma$  is directly related to  $H$  via (1).

The challenge is to obtain the probability curve  $p(\phi)$  from  $F(H)$  by suitable inversion of (5). To do so, the simplest approach is to first generate an analytical form for  $F(H)$  by a curve fit to the measured response for  $F(H)$ , for any value of lithiation  $y$ . Suitable agreement with experiment is obtained upon assuming that the plots of  $F(H)$  vs  $H/H_0$  in Figs. 7a and 7b satisfy the curve fit

$$F - F_0 = (1 - F_0) \left[ 1 - \left( \frac{\frac{H}{H_0} - \alpha}{1 - \alpha} \right)^2 \right]^{\frac{1}{2}} \quad [6]$$

Here,  $H_0$  is the value of substrate hardness that first initiates slip (or fracture) and is dependent upon the degree of lithiation  $y$ ;  $\alpha > 1$  is a fitting parameter with the interpretation that  $F = 1$  when  $H/H_0 = \alpha$ . A best fit gives  $\alpha = 20$  for all values of  $y$ , and  $H_0 = 93$  MPa, 51 MPa and 42 MPa for  $y = 1$ , 0.58 and 0.14, respectively. The derivative  $F'(H)$  follows from (6) as

$$F'(H) = \frac{(1 - F_0) \left( \alpha - \frac{H}{H_0} \right)}{H_0 (1 - \alpha)^2} \left[ 1 - \left( \frac{\frac{H}{H_0} - \alpha}{1 - \alpha} \right)^2 \right]^{-\frac{1}{2}} \quad [7]$$

while  $F'(H)$  follows from (5) as

$$F'(H) = \left[ p(\phi_U) \sin \phi_U + p\left(\frac{\pi}{2} - \phi_U\right) \sin\left(\frac{\pi}{2} - \phi_U\right) \right] \frac{d\phi_U}{dH}. \quad [8]$$

The derivative  $d\phi_U/dF$  is obtained by differentiating (3) with respect to  $H$  such that

$$(2 \cos 2\phi_U) \frac{d\phi_U}{dH} = -\frac{H_0}{H^2} = -\frac{\sin 2\phi_U}{H}. \quad [9]$$

Upon equating (7) and (8) and assuming that  $p(\phi_L) = p(\phi_U)$ , we obtain

$$p(\phi_U) = \frac{2(1 - F_0) \frac{H}{H_0} \left( \frac{H}{H_0} - \alpha \right)}{(1 - \alpha) [\sin \phi_U + \cos \phi_U]} \left[ \frac{\left( \frac{H}{H_0} \right)^2 - 1}{(1 - \alpha)^2 - \left( \frac{H}{H_0} - \alpha \right)^2} \right]^{\frac{1}{2}} \quad [10]$$

upon making use of (3) and (9). For any given value  $1 \leq (H/H_0) \leq \alpha$ , the corresponding value of  $\phi_U$  follows from (3), and the value of  $p(\phi_U)$  follows immediately from (10).

The single value for  $\alpha$  provides a suitable fit for all lithiation states (Fig. 7b), consistent with our expectation that the orientation of particles within a cathode is unchanged by the degree of cathode charge. The inferred shear strength  $\tau_C$  is plotted against the degree of lithiation  $y$  in Fig. 7c, and the distribution of basal plane orientation of particles  $p(\phi)$  as deduced from (10) is plotted in Fig. 7d. Some limiting cases provide insight into this predicted distribution. From

(10),  $p(\pi/4)$  equals  $(1 - F_0) \sqrt{2/(\alpha - 1)}$  and it is this fraction of particles that first slip at  $H = H_0$ . Also, note that the choice (6) of curve fit states that all crystals have slipped,  $F = 1$ , at a finite value of pressure,  $H/H_0 = \alpha$ . Consequently,  $p(\phi)$  vanishes over the small intervals  $0 \leq \phi \leq \phi_L$  and  $\phi_U \leq \phi \leq \pi/2$  where  $\phi_L \approx (1/\alpha)$  and  $\phi_U \approx \pi/2 - (1/\alpha)$  via (3). It is worth mentioning in passing that measured data only extends to  $H/H_0 \approx 10 = \alpha/2$  (Fig. 7b) and thus there is some uncertainty in our estimation of  $p(\phi)$  around  $\phi = \phi_L$  and  $\phi_U$ . However, with  $\alpha = 20$ ,  $\phi_L \approx 0$  and  $\phi_U \approx \pi/2$  this interval of uncertainty is small and therefore does not represent a major drawback to this method as a means of extracting the shear strength of the crystals.

A shear strength  $\tau_C$  of the basal plane under 100 MPa is several orders of magnitude less than the measured Vickers hardness of polycrystalline NMC secondary particles.<sup>15,20</sup> This apparent discrepancy is reconciled by recognising that other ceramic materials, whose atomic structure is similarly layered such as MAX phase compounds, also exhibit shear strengths of their basal plane that are much below both the measured hardness and compressive strength of polycrystalline samples.<sup>32</sup> For example, for the case of  $\text{Ti}_3\text{SiC}_2$ , the critical resolved shear stress<sup>33</sup> required to activate slip on the basal plane is 16.5 MPa. In contrast, the compressive strength<sup>33</sup> of  $\text{Ti}_3\text{SiC}_2$  crystals when loaded in a direction within the basal plane is approximately 4 GPa, and is due to kinking of the lattice layers due to the low shear strength between them. The compressive strength<sup>32</sup> of fine-grained  $\text{Ti}_3\text{SiC}_2$  exceeds 1 GPa, which is some 60 times the shear strength of the basal plane. In the case of polycrystalline NMC samples, the constraints imposed by neighbouring grains preclude their deformation in hardness testing by basal slip alone. General yield requires slip on at least 5 independent slip systems, and a high yield strength of the required secondary slip systems results in a hardness (and uniaxial compressive strength) much above that of the basal plane shear strength.

The shear strength  $\tau_C$  drops rapidly as the  $\text{Li}^+$  ions are removed from the structure and the  $c$ -parameter (and thus interlayer spacing) expands from a Li content of  $y = 1$  to 0.58, recall Fig. 1b. A smaller change in  $\tau_C$  results from additional removal of Li (from  $y = 0.58$  to 0.14), presumably because the interlayer spacing decreases noticeably beyond  $y = 0.35$ , approximately.

The cathode layer of the present study is in the uncalendared state, as is evident by its high porosity. Indentation of the thin uncalendared cathode layer by the Vickers indenter subjects the layer to (i) a normal traction that is sufficiently large that the coating compresses by a large strain in the normal direction, and (ii) to a small transverse strain. The precise stress state within the layer depends upon its constitutive response, and this is unknown for the cathode layer. The simplest idealisation is adopted here, that the “plastic Poisson ratio” is close to zero and so uniaxial stress generates uniaxial strain. This is a reasonable approximation for high porosity solids such as a metallic foams, where a state of uniaxial compressive stress generates a state of uniaxial compressive strain, see for example Deshpande and Fleck.<sup>34</sup> We further note that the assumption of a state of uniaxial compression with vanishing transverse stress leads to a predicted single crystal strength that exceeds the value that would be obtained for the case of a finite compressive transverse stress in the cathode layer. In this sense, the measured single crystal shear strengths of the present study are upper estimates to the actual values.

## Conclusions


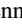
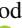
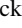
An indentation-based test method has been developed to determine the slip strength of NMC811 single crystals within a porous cathode. The level of imposed compressive stress upon the cathode is dictated by the substrate hardness. By measuring the number fraction of single crystals with visible signs of plastic flow (and/or fracture) as a function of substrate hardness, the compressive stress needed to active plastic flow of the single crystals within the cathode

was determined. The resolved shear strength of the single crystals was deduced from this normal stress, and was found to be  $86 \pm 12$  MPa in the pristine state of a fully lithiated, uncalendered cathode, decreasing to  $39 \pm 5$  MPa upon delithiation (associated with cell charging and loss of the  $\text{Li}^+$  ions which hold the negatively charged metal oxide layers of the cathode together). This low strength suggests that fracture or plastic slip of the NMC811 single crystals might occur because of mild mechanical loading (e.g., via a calendaring operation) or due to mechanical loads generated during electrical cycling of a compacted cathode.

### Acknowledgments

This work was supported by the ERC project “Multilat” under Grant No. 669764, and by the Faraday Institution projects “FutureCat” under grant no. FIRG017 and “Degradation” under grant no. FIRG001 and FIRG024. The authors are grateful to Simon Marshall, Stefan Savage and Daniel Flack of Cambridge University Engineering Department for assisting in the design and manufacture of experimental equipment, and for the assistance of Graham Smith and Len Howlett of Cambridge University Engineering Department with experiments. The authors acknowledge the use of facilities funded by the Henry Royce Institute under grant no. EP/P024947/1.

### ORCID

Joe C. Stallard  <https://orcid.org/0000-0003-2833-0565>  
 Sundeep Vema  <https://orcid.org/0000-0002-9894-5293>  
 David S. Hall  <https://orcid.org/0000-0001-9632-0399>  
 Anthony R. Dennis  <https://orcid.org/0000-0003-4962-7149>  
 Megan E. Penrod  <https://orcid.org/0000-0002-5946-4972>  
 Clare P. Grey  <https://orcid.org/0000-0001-5572-192X>  
 Vikram S. Deshpande  <https://orcid.org/0000-0003-3899-3573>  
 Norman A. Fleck  <https://orcid.org/0000-0003-0224-1804>

### References

1. A. Manthiram, *Nat. Commun.*, **11**, 1550 (2020).
2. S.-T. Myung, F. Maglia, K.-J. Park, C. S. Yoon, P. Lamp, S.-J. Kim, and Y.-K. Sun, *ACS Energy Lett.*, **2**, 196 (2017).
3. A. Kwade, W. Haselrieder, R. Leithoff, A. Modlinger, F. Dietrich, and K. Droeder, *Nat. Energy*, **3**, 290 (2018).
4. F. Pouraghajan, H. Knight, M. Wray, B. Mazzeo, R. Subbaraman, J. Chistensen, and D. Wheeler, *J. Electrochem. Soc.*, **165**, A2644 (2018).
5. T. M. M. Heenan et al., *Adv. Energy Mater.*, **10**, 2002655 (2020).
6. C. Meyer, M. Kosfeld, W. Haselrieder, and A. Kwade, *Journal of Energy Storage*, **18**, 371 (2018).
7. E. N. Primo, M. Chouchane, M. Touzin, P. Vazquez, and A. A. Franco, *J. Power Sources*, **488**, 229361 (2021).
8. C. Meyer, M. Weyhe, W. Haselrieder, and A. Kwade, *Energy Technol.*, **8**, 1900175 (2020).
9. A. C. Ngandjong, T. Lombardo, E. N. Primo, M. Chouchane, A. Shodiev, O. Arcelus, and A. A. Franco, *J. Power Sources*, **485**, 229320 (2021).
10. J. Li, A. R. Cameron, H. Li, S. Glazier, D. Xiong, M. Chatzidakis, J. Allen, G. A. Botton, and J. R. Dahn, *J. Electrochem. Soc.*, **164**, A1534 (2017).
11. J. Li, H. Li, W. Stone, R. Weber, S. Hy, and J. R. Dahn, *J. Electrochem. Soc.*, **164**, A3529 (2017).
12. A. van Bommel and J. R. Dahn, *Electrochem. Solid-State Lett.*, **13**, A62 (2010).
13. E. Trevisanello, R. Ruess, G. Conforto, F. H. Richter, and J. Janek, *Adv. Energy Mater.*, **11**, 2003400 (2021).
14. N. Yabuuchi, Y. Koyama, N. Nakayama, and T. Ohzuku, *J. Electrochem. Soc.*, **152**, A1434 (2005).
15. L. S. de Vasconcelos, N. Sharma, R. Xu, and K. Zhao, *Exp. Mech.*, **59**, 337 (2019).
16. D. J. Miller, C. Proff, J. G. Wen, D. P. Abraham, and J. Bareño, *Adv. Energy Mater.*, **3**, 1098 (2013).
17. J. E. Harlow et al., *J. Electrochem. Soc.*, **166**, A3031 (2019).
18. K. Märker, P. J. Reeves, C. Xu, K. J. Griffith, and C. P. Grey, *Chem. Mater.*, **31**, 2545 (2017).
19. L. Feng, X. Lu, T. Zhao, and S. Dillion, *J. Am. Ceram. Soc.*, **102**, 372 (2019).
20. Y. Bi et al., *Science*, **370**, 1313 (2020).
21. R. Xu, H. Sun, L. S. De Vasconcelos, and K. Zhao, *J. Electrochem. Soc.*, **164**, A3333 (2017).
22. R. Hill, *The Mathematical Theory of Plasticity* (Clarendon, Oxford) (1950).
23. X. Zheng, X. Li, B. Zhang, Z. Wang, H. Guo, Z. Huang, G. Yan, D. Wang, and Y. Xu, *Ceram. Int.*, **42**, 644 (2016).
24. F. H. Allen, G. Bergerhoff, and R. Sievers, *Crystallographic Databases* (International Union of Crystallography, Chester) (1987).
25. V. Marx and H. Balke, *Acta Mater.*, **45**, 3791 (1997).
26. A. K. Bhattacharya and W. D. Nix, *Int. J. Solids Struct.*, **27**, 1047 (1991).
27. D. Durban and N. A. Fleck, *J. Appl. Mech.*, **59**, 706 (1992).
28. A. E. Giannakopoulos, P.-L. Larsson, and R. Vestergaard, *Int. J. Solids Struct.*, **31**, 2679 (1994).
29. A. K. Bhattacharya and W. D. Nix, *Int. J. Solids Struct.*, **24**, 1287 (1988).
30. M. F. Doerner, D. S. Gardner, and W. D. Nix, *J. Mater. Res.*, **1**, 845 (1986).
31. K. L. Johnson, *Contact Mechanics* (Cambridge University Press, Cambridge) (1985).
32. M. W. Barsoum and M. Radovic, *Annu. Rev. Mater. Res.*, **41**, 195 (2011).
33. M. Higashi, S. Momono, K. Kishida, N. L. Okamoto, and H. Inui, *Acta Mater.*, **161**, 161 (2018).
34. V. S. Deshpande and N. A. Fleck, *J. Mech. Phys. Solids*, **48**, 1253 (2000).